Continuous-Flow Synthesis of High-Quality Few-Layer Antimonene Hexagons

Iñigo Torres, Marta Alcaraz, Roger Sanchis-Gual, Jose A. Carrasco,
Michael Fickert, Mhamed Assebban, Carlos Gibaja, Christian Dolle, Diego A. Aldave,
Cristina Gómez-Navarro, Elena Salagre, Enrique García Michel, María Varela,
Julio Gómez-Herrero, Gonzalo Abellán,* and Félix Zamora*

2D materials show outstanding properties that can bring many applications in different technological fields. However, their uses are still limited by production methods. In this context, antimonene is recently suggested as a new 2D material to fabricate different (opto)electronic devices, among other potential applications. This work focuses on optimizing the synthetic parameters to produce high-quality antimonene hexagons and their implementation in a large-scale manufacturing procedure. By means of a continuous-flow synthesis, few-layer antimonene hexagons with ultra-large lateral dimensions (up to several microns) and a few nanometers thick are isolated. The suitable chemical post-treatment of these nanolayers with chloroform gives rise to antimonene surfaces showing low oxidation that can be easily contacted with microelectrodes. Therefore, the reported procedure offers a way to solve two critical problems for using antimonene in many applications: large-scale preparation of high-quality antimonene and the ability to set electrical contacts useful for device fabrication.

1. Introduction

Since the discovery of graphene in 2004,[1] different 2D materials such as hexagonal boron nitride,[2] transition metal dichalcogenides,[3] metal carbides, and nitrides (MXenes)[4] have been prepared because of their outstanding physical and chemical properties and potential technological applications. In fact, despite the extraordinary properties of graphene, its use

for (opto)electronic device fabrication is hindered by the absence of a band gap. In this context, monoelemental materials of group 15 of the periodic table (Pnictogens) have gained increasing attention due to their semiconducting behavior with thickness-dependent band gaps, that can be modulated by strain, doping, or chemical functionalization.[5] Additionally, these 2D-Pnictogens offer unique photonic, catalytic, magnetic, and electronic properties.[6] For instance, black phosphorus (BP) is the first isolated 2D-Pnictogen to exhibit a band gap thickness dependency, ranging from ≈0.3 to 2 eV for bulk and monolayer, respectively, therefore being an excellent candidate for (opto)electronic applications.[7] However, its high reactivity with ambient water and oxygen has prompted the interest in exploring other elements in group 15. Despite arsenene and bismuthene has been successfully prepared by different methods and present interesting properties,[8] antimonene is nowadays the most promising alternative to BP. Antimonene is a monoatomic 2D material with a buckled structure showing exceptional physico-chemical properties suggesting promising applications in top-notch technologies. Although some of its theoretically predicted properties have already been experimentally demonstrated, for example, in supercapacitors[9] or

I. Torres, Dr. C. Gibaja, Prof. F. Zamora
Departamento de Química Inorgánica
Institute for Advanced Research in Chemical Sciences (IAdChem)
and Condensed Matter Physics Center (IFIMAC)
Universidad Autónoma de Madrid
Madrid 28049, Spain
E-mail: felix.zamora@uam.es
M. Alcaraz, R. Sanchis-Gual, Dr. J. A. Carrasco, Dr. C. Dolle,
Dr. G. Abellán
Instituto de Ciencia Molecular (ICMol)
Universidad de Valencia
Valencia 46980, Spain
E-mail: gonzalo.abellan@uv.es

The ORCID identification number(s) for the author(s) of this article can be found under https://doi.org/10.1002/adfm.202101616.

M. Fickert, M. Assebban, Dr. G. Abellán
Department of Chemistry and Pharmacy and Joint Institute of Advanced Materials and Processes (ZMP)
Friedrich-Alexander-Universität Erlangen-Nürnberg (FAU)
Fürth 90762, Germany
D. A. Aldave, Dr. C. Gómez-Navarro, Dr. E. Salagre,
Prof. E. García Michel, Prof. J. Gómez-Herrero
Departamento de Física de la Materia Condensada and Condensed Matter Physics Center (IFIMAC)
Universidad Autónoma de Madrid
Madrid 28049, Spain
Prof. M. Varela
Facultad de CC. Físicas and Instituto Pluridisciplinar
Universidad Complutense de Madrid
Madrid 28040, Spain

for fiber lasers,[10] many others remain a challenge due to the absence of suitable synthetic methodologies to produce the required high-quality material.[11]

Antimonene was first prepared using micromechanical exfoliation, giving rise to mono-layers with limited lateral dimensions.[12] Soon after, different physical methods based on sublimation and on-surface deposition have been developed to provide high-quality antimonene.[11,13] On the other hand, liquid-phase exfoliation (LPE) of antimony has been successfully used to prepare significant quantities of antimonene suspensions.[14] However, we have recently proven that partial surface oxidation occurs during the LPE process hampering the practical use of this material in electronics.[15] Additionally, the chemical synthesis of antimonene has been recently reported using a flash injection method giving rise to the formation of crystalline hexagons of antimonene with nanometric thickness.[16] Although this method provides a significant advance, it is limited to a batch-to-batch synthesis.

Moreover, the antimonene hexagons obtained by this procedure are hampered for some practical applications, for example, (opto)electronics, because of the residual surfactant retained on their surface after the reaction process. Herein, we have performed a systematic study on the experimental parameters governing the chemical synthesis of antimonene hexagons. We have also discovered the tremendous influence of the solvent used on their final surface oxidation. Furthermore, we have designed a continuous-flow synthesis (CFS) that allows the production of high-quality few-layer antimonene (FLA) hexagons in large quantities. The FLAs obtained preserve their physical features, that is, electrical conductivity, thus paving the way for its large-scale production and laying the groundwork for developing antimonene-based electronic devices.

2. Results

When producing antimonene or other 2D materials, it is of critical importance to control features such as the thickness (i.e., number of layers), lateral dimensions, crystallinity, or surface properties. A thorough chemical design turns out to be crucial to study the properties of the material as well as point toward specific applications. In broad strokes, one can divide the methods of synthesizing nanomaterials into two different groups: top–down and bottom–up approaches.[17] In the case of antimonene, both approaches have been reported in the literature. In this context, all micromechanical, liquid phase, or electrochemical exfoliation have demonstrated the ability to produce highly exfoliated antimonene nanoflakes.[12,14a,18] However, one of the main challenges in this sort of synthesis relies on their lack of obtaining well-defined hexagonal morphologies. On the other hand, successful bottom–up approaches such as those based on epitaxial growth (i.e., molecular beam epitaxy (MBE) and van der Waals epitaxy approaches[13]) have led to high-quality antimonene flakes, but fail for the high-scale synthesis of this material.

Herein, we use as a starting point a colloidal bottom–up approach that has been recently reported by Peng et al.[16] In that work, the authors propose the direct synthesis of few-layer and well-defined hexagonal antimonene nanosheets starting from SbCl₃ precursor by promoting their anisotropic growth in a colloidal solution using oleylamine (OA), dodecanethiol (DDT) and 1-octadecene (ODE).[19] Some of the advantages of using solution-phase methodologies rely on their simple procedures, the tunability of the material from the point of view of size, morphology, composition, and the monodispersity of the sample.[20] Therefore, mastering these colloidal approaches allowing CFS may open the door to a large-scale synthesis of antimonene.

2.1. Effects of the Synthetic Parameters on the Colloidal Synthesis of Few-Layer Antimonene Hexagons

The choice for a colloidal route in the synthesis of well-defined hexagonal antimonene allows for overcoming the limitation in the sample quantity characteristic of bottom–up approaches like MBE[13b] and the morphology degradation caused by top–down approaches such as LPE.[14b] Nevertheless, there are some unclear aspects of the precise role of the involved reactants and the exact experimental conditions in some steps during the antimonene colloidal synthesis which remain unclear since this procedure gives rise to a high amount of non-hexagonal morphologies.[16,21] In this sense, by following the same procedure reported in the literature,[16] we obtain hexagonal antimonene flakes with sizes ranging from 1050 to 250 nm and a high amount of Sb non-hexagonal particles (around 50%), but without any noticeable impurity. Transmission electron microscopy (TEM) data of the resulting hexagonal particles, and the respective size distribution histogram, can be found in Figure S1, Supporting Information.

In this context, we have carried out a thorough study focused on the influence of the main experimental parameters during the antimonene formation. By better understanding the formation mechanism, we aim at gaining more control over the particle morphology. The synthetic scheme and parameters under study are depicted in **Figure 1**.

2.1.1. Precursor Solution

In order to prepare the FLA hexagons, it is necessary to reduce the Sb(III) from the SbCl₃ to Sb(0). Surprisingly, we have observed that a partial Sb reduction occurs even during the first step, that is, the synthesis of the Sb(III) precursor. As it can be observed in the X-ray photoelectron spectroscopy (XPS) data shown in **Figure 2**a, peaks corresponding to Sb(0) arise from the Sb spectrum at 528.1 (Sb 3d₅/₂) and 537.4 eV (Sb 3d₃/₂), as well as a new peak at 162.3 eV (S 2p) in the S spectrum which corresponds to a covalent metal-sulphur bonding, which is expected since DDT has been reported to act as a capping agent.[16] These data also point toward DDT being one of the Sb's reducing agents, combined with OA, as stated in the most recent reports.[16,21] As previously described in the synthesis of several perovskites and nanoparticles (NPs) via a similar colloidal approach, OA can act as a reducing agent because of its multifunctionality, as a solvent or as a morphology directing agent, among others.[19b,22]

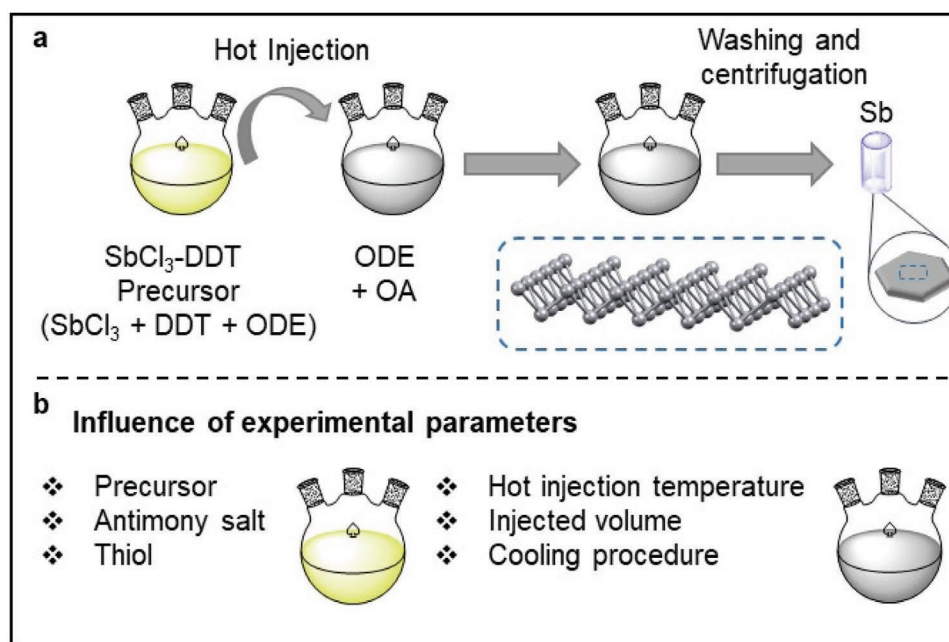Regarding the reduction triggered by the DDT, its thiol groups get oxidized to disulfides, while Sb(III) is reduced to

Figure 1. General scheme of the FLA hexagons preparation process. a) Synthesis of the hexagonal antimonene via colloidal approach. b) Experimental parameters whose influence on the overall reaction is studied.

Sb(0), as evidenced by gas chromatography coupled to mass spectrometry measurement of the precursor solution (Figure S2, Supporting Information), which highlights the appearance of disulfide species. Besides, TEM images suggest the presence of aggregates of small NPs with average sizes of ≈20–50 nm, which are expected to act as seeds for the subsequent formation of anisotropic morphologies such as hexagons (Figure S2, Supporting Information).[23] Besides, by means of energy-dispersive X-ray spectroscopy, the presence of Sb in these NPs was clearly confirmed (Figure S3, Supporting Information).

In this line, the appearance of Sb(0) in the absence of heating motivated us to perform the hot injection of the previously prepared at room temperature $SbCl_3$-DDT solution. As seen in Figure 2b, hexagonal FLAs are obtained even when no heating of the precursor solution is applied. Henceforth, the reduction of Sb(III) by both the thiol reagent and OA, which
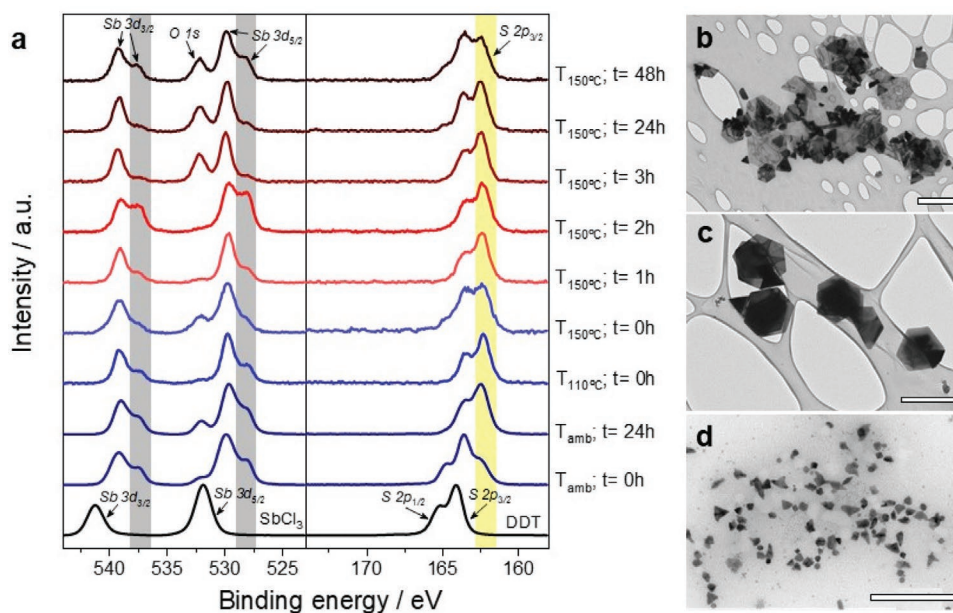

Figure 2. Role of the antimony precursor in the synthesis of few-layer antimonene hexagons. a) XPS spectra of (left) Sb and (right) S at different reaction conditions. Sb(0) and M—S bonding peaks are highlighted in grey and yellow, respectively. b) TEM image of antimonene nanosheets obtained without heating during the first step ($t = 0$ h). Sb particles obtained after precursor reaction times of c) 2 and d) 48 h at 150 °C. Scale bar 1 μm.

takes place already at room temperature, is revealed as a crucial step for obtaining the hexagonal morphology. In this context, it is of utmost importance to carefully degas the reagents for at least 12 h before starting the reaction to avoid the presence of any impurities in the final material. Nevertheless, the absence of heating during the first step gives rise to hexagonal nanosheets with lateral dimensions of 800 ± 300 nm (Figure S4, Supporting Information). Still, with a high number of undesirable morphologies, only 33% of the particles are hexagons. In fact, as shown by XPS (Figure 2a), Sb—S bonding peak increases by applying temperature, and the amount of Sb(0) reaches its maximum after heating at 150 °C for 2 h. Thus, optimum conditions are achieved by heating the precursor solution at 150 °C for 2 h after purifying the reagents. TEM confirms the presence of well-defined hexagonal nanosheets with a lower number of irregular morphologies (Figure 2c). Nevertheless, if the synthesis time continues increasing up to 48 h, this leads to the formation of many irregularly shaped antimony particles of ≈50 nm and the absence of any hexagonal nanosheets (Figure 2d). In line with that, different times were also tested during the additional heating steps in the synthesis of the SbCl₃-DDT precursor, that is, the heating time at 60 °C before the hot injection phase. In this context, heating at 60 °C for longer times than 1 h leads to quite similar hexagonal nanosheets (Figure S5, Supporting Information). Therefore, adequate precursor formation is revealed as a crucial step in the formation of the resulting structure; however, the heating time before hot injection does not play a critical role.

2.1.2. Antimony Salt

In order to analyze the influence of the antimony salt on the overall morphology of the resulting antimonene, two different additional reagents were tested as the primary sources of antimony, namely $Sb(AcO)_3$ and SbF_3. As has already been reported, the combination of the antimony salt $Sb(AcO_3)$ and dodecyldimehtylammonium bromide gave rise to hexagonal nanosheets.[16] Here, the use of only $Sb(AcO)_3$ does not lead to the growth of hexagonal nanosheets, but the formation of NPs of about 100 nm (Figure S6, Supporting Information). Additionally, if the growth time is extended up to 120 s, the small particles evolve to antimony tetrahedrons of ≈350 nm in size. On the other hand, the use of SbF_3 resulted in NPs having irregular morphology with an average size of 100 nm at 10 s of growing time (Figure S6, Supporting Information). According to these results, the most prominent finding is that halogenated salts are not the sole condition to obtain the final hexagonal shape.

2.1.3. Thiol

Due to the synthetic conditions and the heating step at 150 °C, the selected thiol must exhibit a boiling point above that temperature. This feature neglects simple thiols with an alkyl chain lower than 12 carbons. Nevertheless, a thiol larger than DDT was used to analyze the influence of the organic ligand in the formation of the hexagonal morphology. Therefore,

octadecanethiol (ODT)[24] was tested. In this synthesis, the preheating temperature before the hot injection was set at 72 °C, instead of the typical 60 °C, due to the higher melting point of the ODT compared to the DDT. When the SbCl₃-ODT was chosen as the precursor, the results were in good agreement (in terms of morphology) with the expected hexagonal nanosheets found in the case of SbCl₃-DDT (Figure S7, Supporting Information). Nonetheless, the resulting hexagonal antimonene exhibited smaller average lateral dimensions of ≈300 nm, half the size of the hexagons synthesized with DDT. This fact highlights the importance of the thiol ligand for the formation of the desired morphology since the absence of DDT or ODT gives rise to non-hexagonal particles[16] while showing a route to obtain FLA hexagons of smaller sizes.

2.1.4. Hot Injection Temperature

The hot injection temperature shows up as a critical parameter during the synthesis of the FLA hexagons. However, although the typical synthesis is carried out at 300 °C during the hot injection step, lower and higher temperatures have also been tested. The resulting hexagons exhibit a clear dependence of the lateral dimensions with the temperature. While 280 °C gives rise to smaller hexagonal flakes (200 ± 100 nm), 320 °C leads to larger hexagons of 1300 ± 400 nm but with a higher degree of polydispersity as well as irregular morphologies (Figure S8, Supporting Information). It is also noticeable that an increase in the injection at temperatures up to 320 °C (Figure S8d,e, Supporting Information) leads to the presence of nanorods corresponding to Sb_2O_3.[25] These Sb_2O_3 will be further highlighted and characterized in Figure S12, Supporting Information. Therefore, lowering the hot injection temperature produces FLA hexagons of a few hundred nanometers in lateral dimensions.

2.1.5. Injected Volume

In general, parameters such as concentration and metal/surfactant ratio strongly affect the size of NPs. It was found that the reduction of the metal concentration usually leads to larger NPs. Therefore, the purpose of the present study was to vary the amount of SbCl₃-DDT precursor solution to maximize the lateral dimensions of the hexagonal nanosheets while keeping constant the amount of the OA (0.5 mL) and ODE (4.0 mL) mixture. In a typical synthesis, 1 mL of SbCl₃-DDT solution is injected during the hot injection. Both decreasing and increasing the injected volume (0.5, 0.7, and 2 mL of Sb precursor) leads to the formation of FLA hexagons. Figure S9, Supporting Information shows that there are clear differences among the tested volume: lower quantities give rise to larger particles of ≈1.2 μm in lateral size (1.1 ± 0.3 and 1.3 ± 0.4 μm for 0.5 and 0.7 mL, respectively). The larger size can be ascribed to the smaller quantity of nucleation seeds, as reported in the literature, to grow NPs.[26] Regarding the percentage of hexagonal versus non-hexagonal particles, we have estimated a 30% and 35% ratio for 0.5 and 0.7 mL, respectively. On the other hand, the sample with 2 mL of injected volume gives rise to the smallest

antimonene hexagons with an average size of 500 ± 100 nm but with the highest percentage of hexagonal morphologies reaching 70% compared to non-hexagonal shapes (Figure S9, Supporting Information). With this in mind, 1 mL precursor addition seems to be an ideal condition to get a higher yield of hexagonal morphology (70%) with larger dimensions, ranging from ≈1050 to 650 nm.

2.1.6. Reaction Time and Cooling Procedure

The reaction time is one of the most critical parameters in the synthesis of FLA hexagons and the most challenging to control since differences of just a few seconds can significantly affect the quality of the final product. In this sense, a parameter that severely affects the crystallization process is the cooling-method after the reaction takes place. According to work already published,[16] the growth of these NPs preferentially occurs at 300 °C on the basal facet of the nanosheets. The evidence from this study suggests that if the antimonene nanosheets are quickly cooled down to room temperature, thinner and monodisperse hexagonal nanosheets could be obtained. We have analyzed the differences between reducing the reaction temperature from 300 to 50 °C using a dry ice bath (≈1 min) versus allowing the reaction to reach 50 °C under ambient conditions (≈5 min). The resulting TEM images can be seen in Figure S10, Supporting Information, pointing out the well-defined hexagonal morphology obtained in both approaches (slow and fast cooling). Furthermore, we have seen that when the cooling-time becomes shorter, the FLA hexagons show lower lateral dimensions of ≈900 nm compared to those obtained with longer cooling-times (≈1400 nm). When using a dry ice bath, the reaction abruptly stops, avoiding the FLA growth in all directions. This observation agrees with a conventional crystallization process in which a lower rate in the decrease of the temperature produces larger crystals. In contrast, a faster process provokes the formation of more nuclei giving rise to smaller crystal sizes.

Therefore, we carried out new experiments to maximize the lateral dimensions without increasing the hexagon thickness. To do so, we study the slow cooling method when the reaction was stopped at $t = 0$ s, 10 s, and 2 min. We have observed that the optimal results are obtained when the reaction is stopped immediately after the precursor is injected (denoted as $t = 0$ s). Thus, for instance, longer reaction times, for example, 10 s, give rise to FLA hexagons of shorter lateral dimensions while the height, measured by AFM, dramatically increases from ≈5 to 70 nm upon increasing the reaction time (Figure S11a,b,d,e, Supporting Information). These observations agree with forming a larger amount of Sb(0) after a longer reaction time (10 s vs 0 s) that provokes more crystallization nuclei giving rise to smaller crystal sizes. We have also observed that longer reaction times (2 min) produce thicker and shorter FLA hexagons together with stick-like morphologies that correspond to antimony oxide of a side oxidation reaction, as confirmed by Raman spectroscopy showing peaks at 187, 254, and 450 cm^{-1} (Figures S11c,f, S12, Supporting Information).

Therefore, the minimum height measured by AFM (overestimated the material thickness[14a]) in these experiments for FLAs was 5 nm, using the shorter reaction time and slow cooling.

Figure S13, Supporting Information summarizes the optimized experimental parameters found to produce the best-defined FLA hexagons with larger lateral size dimensions. These parameters combine the use of antimony chloride salt with a long-chain thiol such as DDT or ODT under an inert atmosphere (Ar), followed by 2 h heating at 150 °C. Afterward, the precursor can be stored at 60 °C. Concerning the hot injection step at 300 °C, 1 mL is found to be the optimum volume needed for the successful synthesis of high-quality hexagonal nanosheets. Then, an aggressive cooling with dry ice leads to a reduction of the lateral dimensions. On the other hand, slow cooling in combination with an abrupt stopping of the reaction at $t = 0$ results in large lateral sizes without compromising the thickness.

2.2. Morphological and Spectroscopic Characterization of Few-Layer Antimonene Hexagons

With the synthetic methodology previously reported, well-defined FLA hexagons were obtained.[16] Hitherto, with our optimized experimental parameters, we have been able to synthesize pure thin antimonene hexagons with lateral dimensions up to several microns. Specifically, flakes of ≈900 nm are obtained (40% bigger than the reported particles), exhibiting higher monodispersity (deviation of 300 vs 400 nm). A typical flake obtained with our optimized procedure as observed under the optical microscope and the atomic force microscopy (AFM) is shown in **Figure 3**a,b, respectively. The antimonene flake exhibits a perfect hexagonal structure with a flat and relatively smooth surface. The height profile extracted from the AFM data displays a thickness of 5 nm with a lateral size of 2.8 µm (Figure 3a). Statistical analysis of the height and length of produced hexagons is shown in Figure S14, Supporting Information, considering only the flakes with a thickness no exceeding 20 nm. The structure of the hexagonal flakes was investigated using scanning Raman microscopy. Spatial mapping of the characteristic A$_{1g}$ mode with a step size of 200 nm has yielded the Raman map shown in Figure 3b, which is in perfect correlation with the optical and AFM images. The mean Raman spectrum of the whole antimonene hexagon was extracted and compared to the Raman spectra of the bulk Sb (Figure 3c). In the bulk Sb, the two main vibrational modes of bulk antimony can be seen at 112 cm^{-1} (E$_g$) and 150 cm^{-1} (A$_{1g}$), ascribed to the in-plane and the out-of-plane vibrations, respectively. While in the case of the 5 nm FLA hexagons, the same Raman modes are observed at 140 and 168 cm^{-1}, respectively, thus revealing a pronounced blue shift (28 cm^{-1} for the E$_g$ mode and 18 cm^{-1} for the A$_{1g}$ mode), in perfect agreement with previous theoretical predictions as well as recent experimental observations.[14a,27] Additional AFM images of antimonene hexagons with thicknesses of 6–8 nm and their corresponding average Raman spectra are shown in Figure S15, Supporting Information. Moreover, TEM images of the as-synthesized material can be found in Figure S16, Supporting Information.

The produced FLA hexagons exhibit larger lateral dimensions than those produced with top–down approaches, such as LPE and scotch-tape method, and have thicknesses comparable to those made using chemical vapor deposition or MBE. This
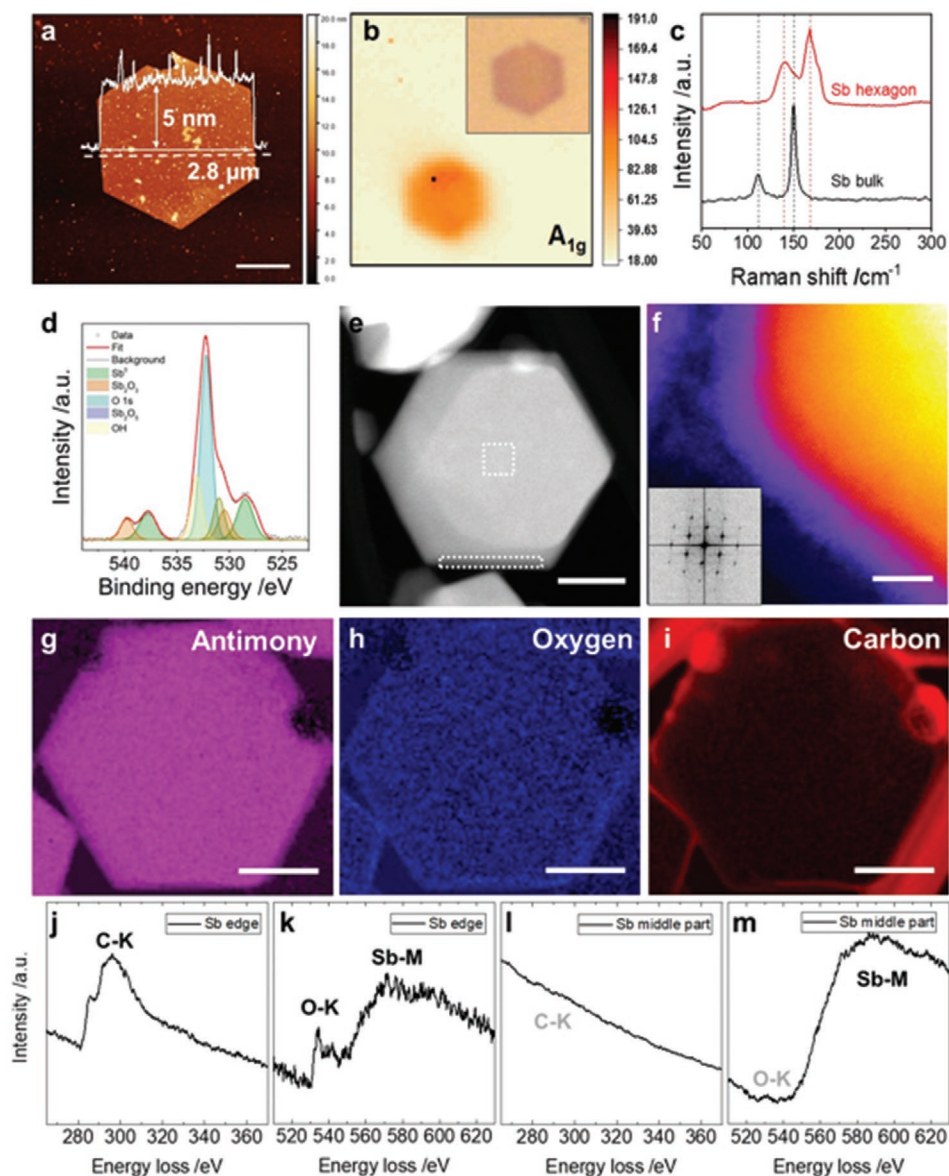
Figure 3. Morphological and spectroscopic characterization of few-layer antimonene hexagons. a) AFM profile of individual Sb nanosheet with overlaid thickness profile (5 nm height over 2.8 μm diameter). Scale bar of 1 μm. b) Raman mapping of A_{1g} (150 cm^{-1}) intensity with optical micrograph given as inset. c) Comparison of the Raman signal of bulk antimony and the Sb hexagonal nanosheet. d) Typical XPS line spectra of Sb 3d 5/2 and 3/2 region for Sb hexagonal nanosheets (under environmental conditions) showing contributions from both metallic and oxidized Sb components. Individual contributions from the fitting are highlighted. e) HAADF STEM image of individual nanosheet with indicated regions in the center and at the rim of the flake used for the extraction of EEL spectra in Figure 2j–m. f) Colorized high resolution STEM-HAADF image to emphasize the amorphous edge surrounding the particles. Inset shows the FFT demonstrating the crystallinity of the material. Scale bar of 5 nm. g–i) Elemental compositional EELS maps (Sb M$_{4,5}$, O K, and C K) of the hexagon shown in (e). Scale bar (e–i) of 100 nm. j–m) Comparison of EELS signatures of the nanosheet extracted from the edge and the inner region of the crystal. Carbon and oxygen are highly enriched at the edge, indicating terminal oxidation and residual carbonaceous material presumably from the synthesis acting as a capping layer. In the central part of the crystal, the amount of carbon and oxygen is strongly reduced and not measurable.

technique stands out by allowing comparatively larger quantities while maintaining excellent morphological and structural quality.

Another essential aspect that should be considered is the surface chemistry of the FLA hexagons, even more so when it comes to synthetic methods based on wet chemistry. In this sense, XPS reveals the presence of Sb^0 plus significant surface

oxidation (Figure 3d). The native oxidation layer is further confirmed by aberration-corrected scanning TEM (STEM) and electron energy-loss spectroscopy (EELS).

A high-magnification high angle annular dark field (HAADF) image near the edge of the nanosheet is displayed in Figure 3f with the fast Fourier transformation (FFT) depicted as the inset. The FFT distinctly demonstrates the high degree of

crystallinity, and from the image data, no significant defects within the nanosheet can be observed. In the colorized high-resolution HAADF image, the presence of a nanometric (3–5 nm) thick amorphous layer at the edges of the nanosheet becomes visible. The amorphous rim shows an increased EELS signature in regard to carbon and oxygen (Figure 3j,k), while these elements cannot be measured in the central part of the crystal (Figure 3l,m). The chemical composition of the sample was determined by EELS over the hexagon shown in Figure 3e, which allowed the construction of the Sb $M_{4,5}$, O K, and C K elemental maps as depicted in Figure 3g–i. The hexagon is mainly composed of Sb and a noticeable amount of oxygen located at the surface and edges of the nanosheet, indicating a native oxidation layer of Sb_2O_3.[15,27,28] Additionally, a significant C signal was detected on the edges of the nanosheet, most probably as a result of the presence of capping agents as well as contamination from residual solvents.[29] The presence of S was not detected on the surface, in good agreement with XPS and thermogravimetric analysis coupled to gas chromatography and mass spectrometry (TG-GC-MS), in which ODE, OA, and 9-octadecenenitrile (an impurity from the OA) were the predominant species detected (Figure S17, Supporting Information).

2.3. Upscaling the Reaction

Once these optimal synthetic parameters have been established, our focus was on determining whether antimonene production can be scaled up, as these types of batch-to-batch reactions usually provide very low yields. Then, we study the possibility of scaling up the reaction to obtain higher amounts of antimonene. First, we increased the concentration of all components by a factor of two and ten. Both cases lead to the successful synthesis of FLA hexagons (Figure S18, Supporting Information), but if the scale-up factor increases from ×2 to ×10, larger quantities of additional irregular shaped particles are found. Alongside that, we also observed some issues related to the homogeneity of the sample. In this context, the average size of the nanosheets after the upscaling processes exhibited extremely polydisperse sizes (i.e., 700 ± 200 and 1500 ± 700 nm for scaling up by a factor of 2 and 10, respectively). Besides, the percentages of observed hexagons were 44% and 36% for the ×2 and ×10 samples, evidencing a more significant amount of non-hexagonal morphologies as the scaling process goes up (Figure S18, Supporting Information). This major polydispersity could be associated with the cooling method, which is not effective with such high volumes. Henceforth, a simple and scalable method solely based on increasing the reagent quantity is not possible, and alternative strategies are highly desirable.

2.3.1. Continuous-Flow Synthesis

To avoid the scale-up issue, we decided to explore a CFS approach using a continuous-flow reactor. We used a home-made tubular stainless-steel reactor consisting of a 50 cm long tube with inner diameter of 6 mm (see Experimental Section for details) as schematically represented in **Figure 4**a and Figure S19,

Supporting Information. Optimizing the CFS synthetic parameters requires the readjustment of some of the parameters used in the batch method. Indeed, in the continuous synthesis, we do not use the hot injection method, but instead, the precursor and reaction medium are mixed at 30 °C before introducing the mixture in the tubular reactor. This modification directly affects the reaction temperature, which decreases from 300 °C used in the hot injection method to 250 °C in the continuous one. We have noted that further reduction of the reaction temperature produces a significant decrease in the reaction yield or the absence of this process (below 200 °C). We have also observed that the use of temperatures over 250 °C promotes the appearance of stick morphologies corresponding to antimony oxide (Sb_2O_3), as has been explained before (Figure S12, Supporting Information). Finally, the reaction product is collected and cooled down under ambient conditions to stop the antimony growth. Then, the suspension is centrifuged and washed up with chloroform to isolate the FLA hexagons for further characterization.

Figure 4b shows a typical AFM image of an FLA flake with its characteristic hexagonal morphology. The flake shows ≈4.5 µm in lateral dimensions and 5 nm in thickness. The morphology and thickness of the FLA hexagons show good homogeneity in size and shape (Figure S20, Supporting Information). With the aim of obtaining information about the area and the thickness distribution of the synthesized FLA hexagons, we have performed a statistical AFM study on 120 FLA hexagons. Figures S21,S22, Supporting Information show that the lateral size varies from 0.5 to 6 µm, with areas over ≈2.5 µm², and most of the flakes show a thickness below 20 nm. An inversely proportional relationship between the area and the thickness is also observed. This suggests that the FLAs present a similar mass with preferential growth in the basal plane. Stability of FLA hexagons was confirmed by AFM (Figure S23, Supporting Information). Figure 4c shows a TEM image of a typical FLA hexagon obtained by the continuous method confirming that the morphology is similar to those FLA hexagons obtained in the flask injection discontinuous approach (Figure S24, Supporting Information). The diffraction pattern recorded on the same FLA flake obtained in the continuous process and shown in Figure 4c, presents the hexagonal ordering characteristic of the rhombohedral atomic structure. The single point Raman spectrum of an FLA flake with 60 nm of thickness, excited at 532 nm, reveals the representative main phonon peaks, the A_{1g} mode at 149.8 cm^{-1} and E_g mode at 110.0 cm^{-1} (Figure 4d). However, the single point spectrum of an 8 nm thick FLA hexagon shows a significant blue shift exhibiting the A_{1g} mode at 160.1 cm^{-1} and E_g mode at 125.8 cm^{-1}, which agrees with recent reports.[30] Furthermore, in the same way as was done for the samples prepared by hot injection (Figure S15, Supporting Information)—a study was carried out on six FLA hexagons of different thicknesses that confirmed the increase in a blue shift as the thickness decreases (Figure S25, Supporting Information). Additionally, Figure 4e shows the X-ray powder diffraction (XRPD) pattern of the FLA hexagons featuring diffraction peaks indexed to rhombohedral β-phase of antimony (JCPDS No. 35-0732), suggesting the high purity of the reaction product. We do not observe any significant change in both Raman spectra and XRPD of FLA hexagons storage under ambient conditions, suggesting material stability (Figure S26, Supporting Information).
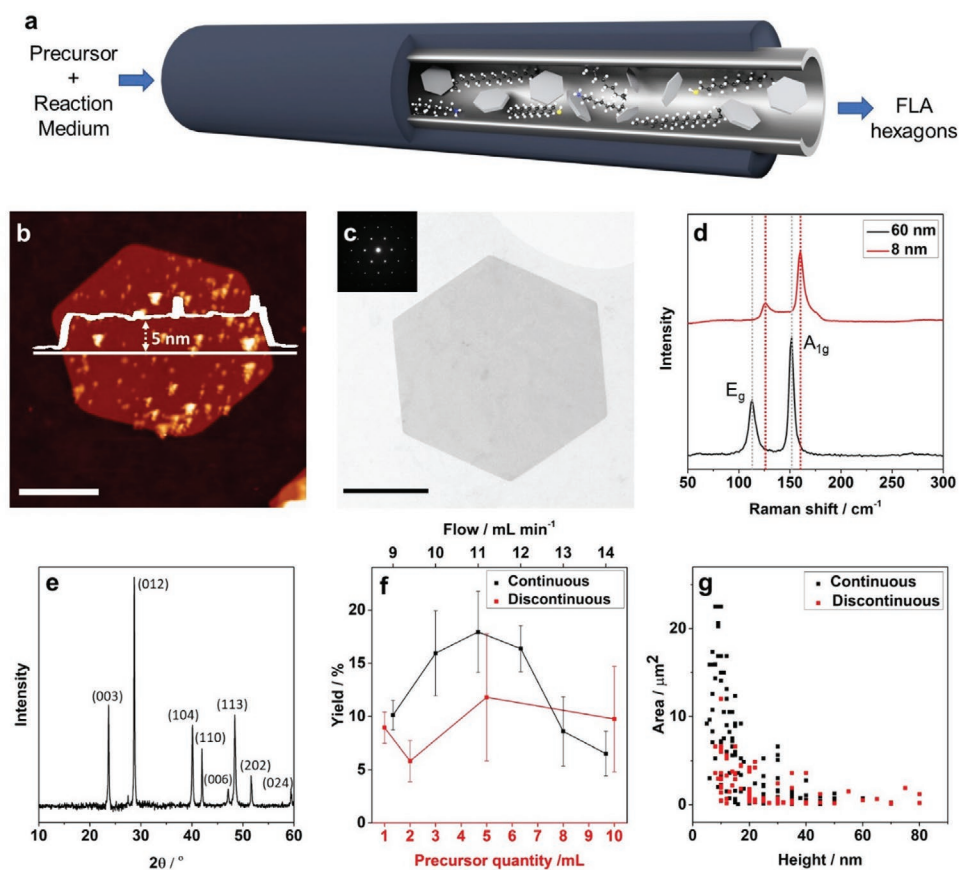
Figure 4. Continuous-Flow Synthesis of few-layer antimonene hexagons. a) Schematic representation of the FLA synthesis by a continuous process. b) AFM image of an FLA hexagon showing the height profile of ≈5 nm. Scale bar of 1.5 μm. c) TEM image of FLA hexagon synthesized by the continuous method. Scale bar of 1 μm. d) Raman single-point spectra of two FLA hexagons whose thicknesses are 60 and 8 nm, respectively. e) XRPD pattern of the powder of FLA synthesized by the continuous procedure. f) Plot of the yields as a function of the flow in the continuous process and amount of precursor in the discontinuous process. g) Plot of the area as a function of the height of the FLA hexagons synthesized by both continuous and discontinuous procedures.

The optimized synthetic parameters for the continuous process use reactant flow rates between 9 and 14 mL·min^{-1}. We have observed that lowering the reaction flow provokes the appearance of antimony oxide sticks while increasing the flow induces a significant reduction in the reaction yield. The optimized reaction parameters give rise to a maximum yield close to 18%, at 11 mL·min^{-1}, which is significantly higher than the best yield obtained with the batch method (12%; Figure 4f). Using this flow, we produce ≈0.964 mg h^{-1}. For comparison, we have optimized the yield for the discontinuous batch method. Figure 4f shows that the maximum yield is achieved when the reaction is carried out with 5 mL of the precursor, while a decrease in the reaction yield is observed as far as the amount of reactants increases. Therefore, this is a clear limitation to the scale-up of FLA hexagons preparation on a much larger scale. In addition, the typical deviation of the yields is far higher in the batch method, which implies that the reproducibility of the process in terms of yield is very low. Figure 4g shows the relation between the area and the thickness of the FLA hexagons obtained using the conditions to get the best yield in the two different methods. In both cases, it can be seen the inversely proportional relationship between the area and the thickness

commented before (Figures S21,S22,S27,S28, Supporting Information). When the synthesis was carried out in a continuous way, the FLA hexagons present larger areas and lower thicknesses, which implies the formation of a more defined 2D material.

2.4. Post-Synthetic Treatment versus Oxidation

After the continuous process, the obtained FLA hexagons are covered with capping agents as well as contamination from residual solvents.[29] In order to isolate FLA hexagons, we thoroughly washed them to remove any contamination from reaction solvents and surfactants. Thus, we have observed interesting differences between the use of chloroform or isopropanol as washing and redispersing solvents to prepare FLA dispersions. We have selected these solvents because they represent some of the most used solvents to obtain FLA dispersions.[14b]

2.4.1. Surface Characterization

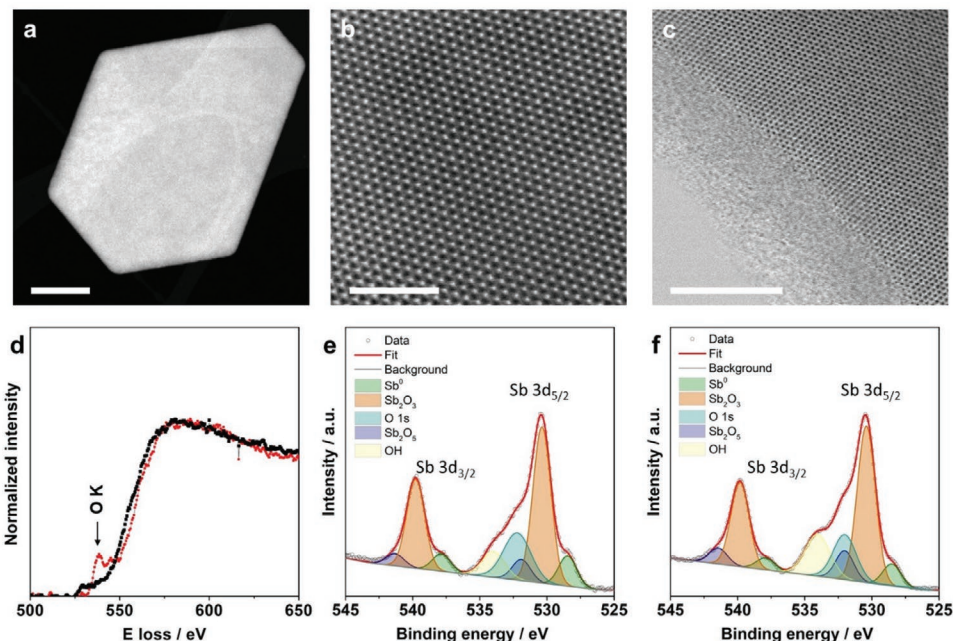The HAADF image of the FLA hexagons washed with chloroform confirms that they are flat and exhibit hexagonal shape

Figure 5. Morphological, structural, and surface characterization of few-layer antimonene. a) HAADF image of FLA hexagon acquired at an acceleration voltage of 80 kV. Scale bar of 200 nm. b) High-magnification annular bright field (ABF) image of the material surface showing the high degree of crystallinity. Scale bar of 2 nm. c) ABF image near the edge of the FLA hexagon showing the amorphous few nanometers thick layer at the flake edge. Scale bar of 5 nm. d) EEL spectrums of FLA hexagon dispersed in chloroform (black) and dispersed in IPA (red). e) Typical XPS line spectra of FLA hexagons synthesized by continuous procedure dispersed in chloroform. f) Typical XPS line spectra of FLA hexagons synthesized by continuous procedure dispersed in IPA.

(**Figure 5**a). Furthermore, a high-magnification annular bright field (ABF) image of the material surface (Figure 5b) shows the high degree of crystallinity, with the (111) direction coming out of the plane of the 2D flakes. Moreover, no significant defects or secondary phases are observed. However, the edges exhibit a nanometric thick amorphous layer, as observed in the ABF images (these are more sensitive to local crystallinity), and very likely this layer affects the top and bottom surfaces, very similar to that shown above for hexagons made by hot injection (Figure 5c). A similar morphology and crystallinity is observed in FLA flakes washed with isopropyl alcohol (IPA), and a few nm thick layer is again observed at the flake edges (Figure S29, Supporting Information). EEL spectrum images exhibit a small degree of oxidation, in the form of a small O K edge contribution, in both FLA hexagons washed with chloroform and with IPA (Figures S30b,d, S31b,d, Supporting Information). Unfortunately, it is not possible to carry out an O/Sb relative composition quantification due to the overlap of the O K and Sb $M_{4,5}$ edges (Figures S30c,S31c, Supporting Information). Interestingly, a comparison of the EEL spectra between those FLA flakes washed with chloroform to those washed with IPA shows that EEL spectra exhibit more intense O K edge features in the IPA sample (Figure 5d, red line), pointing to a slightly higher oxidation degree on the surface of the flake than the sample in chloroform (Figure 5c, black line).

In order to study the composition of FLAs at the surface level, we have used XPS. The results of the FLA flakes deposited on highly oriented pyrolytic graphite surfaces (Figure 5e) reveal the presence of antimony oxides besides metallic antimony.

The O 1s peak is also detected, as it happens to appear very near to Sb 3d. It includes a component related to antimony oxides (at 532.1 eV) and a component associated with OH (at 534.0 eV). This is due to the exposure of the sample to the atmosphere before performing XPS. As it can be observed in the XPS, the FLA hexagons present more antimony oxide in those samples redispersed in IPA rather than in those redispersed in chloroform, in agreement with EELS. The composition of the antimony oxide layer is also different, with approximately 35% more Sb_2O_5 (at 531.9 eV) in the case of samples dispersed in IPA than in samples dispersed in chloroform. The Sb_2O_3 fraction (at 530.4 eV) is the same in both cases. Furthermore, the samples dispersed and sonicated in IPA have a significantly smaller metallic antimony peak (39% less) compared to samples dispersed in chloroform (Figure 5f). These results agree with the oxidation study reported in FLA hexagons prepared by LPE. It shows that the chemical synthesis method provides FLA flakes with less surface oxidation due to the metallic antimony peak being significantly higher.[15]

2.4.2. Mechanical and Electrical Properties

Electron microscopy, Raman, XPS, and AFM strongly suggest a high degree of crystallinity and purity for the synthetized FLA hexagons. However, it is not clear to what extent the hexagonal flakes preserve their mechanical properties. To gain information on this aspect, we have performed for the first time nanoindentations on both types of Sb flakes, synthetized FLA hexagons, and
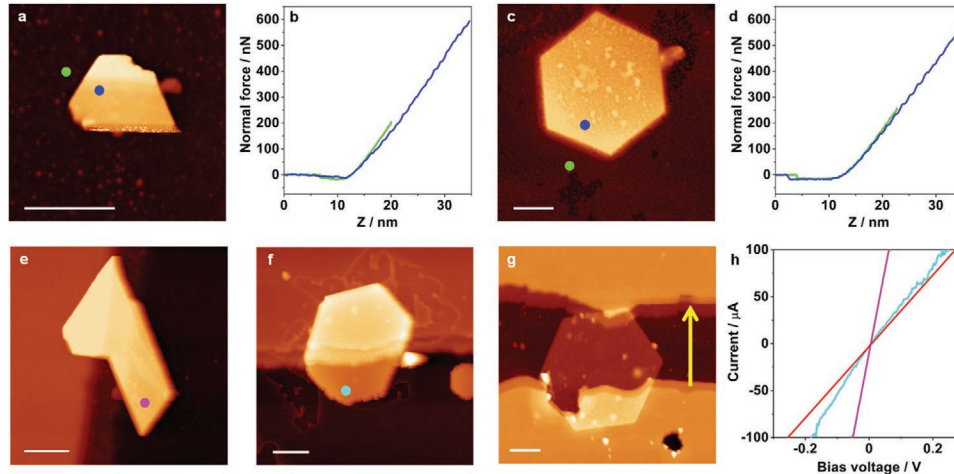
Figure 6. Mechanical and electrical characterization of FLA hexagons. a) AFM topography image showing an antimony microexfoliated flake on SiO_2. In the image, it is marked the tip-sample contact point on the substrate (green dot) and on the flake (blue dot). Sale bar correspond to 1 μm. b) Force versus distance plots performed at the regions pointed by dots in (a). c) AFM topography image showing a FLA flake on SiO_2. In the image, it is marked the tip-sample contact point on the substrate (green dot) and on the flake (blue dot). d) Force versus distance plots performed at the regions pointed by dots in (c). e) AFM topography image of a microexfoliated antimonene flake on SiO_2 with an average thickness of 100 nm connected to a gold electrode (left region) for cAFM measurements. f) AFM topography image of a FLA flake on SiO_2 with 90 nm average thickness connected to a gold electrode (upper region) for cAFM measurements. g) AFM topography image of a FLA flake with 16 nm thickness connected to a pair of gold microelectrodes (lower and upper regions; the yellow line indicates the flow of current for the red *IV* curve). h) Current versus voltage characteristics for: violet (e), cyan (f), and red (g) lines. FLAs showed in (f,g) were resuspended in chloroform. The dots in (e,f) point to the *IV*s contact region in the cAFM measurements.

those obtained by microexfoliation. More specifically, we select random spots on the flake surfaces, and then we indent the AFM tip loading the sample up to a maximum force. **Figure 6**a shows an AFM topography image of a microexfoliated flake with dots pointing to the areas where nanoindentations were done. Figure 6b portrays a force versus distance curve where the cantilever bending, hence the applied force, is basically the same as in the silicon oxide substrate. The same situation is observed in FLA flake (Figure 6c,d), where indeed both coincide within the experimental error. According to Hertz's model the maximum contact pressure P_{max} between the AFM tip and the sample is about 5 GPa (Section S3, Supporting Information for additional details). Magnification of the topographies AFM images in the region where we performed the force versus distance plots show no traces of damage on the surface of the flake, confirming the strength of the FLA.

On the other hand, it has been already reported that LPE of antimony gives rise to FLA in which a passivation oxidation layer and antimony oxide is formed at the surface level.[15,31] We have observed that the insulating nature of the antimony oxide prevents a good electric contact hampering the electrical characterization of the antimonene layers so-produced. However, the obtained results suggest the possibility of establishing electrical contacts to characterize the FLA surface electrical conduction. To this end, we have initially carried out two electrode experiments with conductance AFM in exfoliated flakes (Figure 6e) and FLA redispersed in chloroform (Figure 6f) with similar thicknesses of about 90 nm (Methods S4, Supporting Information for additional details). The corresponding current versus voltage characteristics (*IV*s) exhibit lower conductance for the FLA hexagon than for the microexfoliated one (Figure 6h blue and green curve, respectively). As the thicknesses of the flakes

are similar, we attribute this result to the different contact resistances between the flakes and the electrodes. Contact resistance is always present in electrical transport measurements and is a major concern in nanosystems.[31] Therefore, we confirm that the FLAs prepared by our CFS method can successfully be electrically contacted. Notably, the *IV* curves are linear as expected for metal contacts. These experiments strongly suggest that FLA hexagons exhibit excellent electrical conductance comparable to that of microexfoliated flakes.

We confirmed these results further by performing electrical transport measurement with an alternative experimental set up where we connected a 16 nm thick FLA flake to a pair of microelectrodes evaporated using a stencil mask (Figure 6g; Figure S32, Supporting Information). In this case, the flake does not withstand any kind of mechanical pressure, as in the case of conductive AFM (cAFM). The corresponding *IV* (red line in Figure 6h) shows a clear linear tendency with a low electrical resistance of 2.5 kΩ, including the contact resistance, confirming the cAFM measurements again.

We applied the same methodology for electrical characterization of FLA redispersed in IPA with negative results (Figure S33, Supporting Information). This evidence further confirms the growth of an insulating layer on top of the flake, preventing electrical contact.[31]

3. Conclusion

A thorough analysis of the experimental parameters involved in the colloidal synthesis of antimonene hexagonal nanosheets has been carried out. The optimized conditions have been established by means of a combined characterization involving

XPS, HRSTEM-EELS, AFM, Raman spectroscopy, TG-GC-MS, and XRD. We have demonstrated that the control of the experimental conditions allows the formation of FLA hexagons with lateral dimensions that can be modulated from ≈200–300 nm to 2–3 microns, allowing selecting the material size for each specific application, for example, biomedical, (opto)electronics, catalysis or energy storage, to name a few.

However, this conventional batch-to-batch synthetic approach is restricted to low yields and cannot be scaled up. To face this challenge, we developed a continuous flow synthesis that allows the large-scale production of antimonene nanosheets with excellent morphological and structural quality. Indeed, our optimized synthesis yields antimonene hexagons with lateral dimensions up to 6 microns—larger lateral dimensions than those produced with top–down approaches, such as LPE and scotch-tape methods and thicknesses in between 4 and 20 nm, comparable to those made using chemical vapor deposition or MBE. Furthermore, the high quality of these chemically produced antimonene hexagons is reflected in their mechanical properties and the low degree of surface oxidation, allowing the nanosheets to be successfully contacted with microelectrodes.

The literature already envisions different potential applications for antimonene.[9,10] Some of them require relatively large amounts of antimonene even to prepare devices at the lab scale (e.g., supercapacitors, biosensors, drug delivery, catalysis, etc.), and those applications can hardly be satisfied with existing technologies (i.e., LPE). Moreover, applications requiring good electrical contacts cannot be performed with LPE antimonene flakes due to the presence of oxidation layers on the top of antimonene surface,[15] and more sophisticated technologies such as MBE are required. However, these processes can hardly be scaled up.

Additionally, the current size of the FLA hexagons here reported covers some microns (up to 6 μm), despite these are still sizes relatively small for some specific applications in which continuous films are necessary, but surpass the flakes obtained using MBE, LPE, or micromechanical exfoliation. Moreover, our FLA hexagons are large enough for some realizations, such as micro-sensors or FETs.

In summary, this work plays a crucial role in providing an alternative preparation with the higher yields reported to date. These results open the door for the development of antimonene-based technologies since it allows for the first time the large-scale synthesis of high-quality nanosheets for applications in electronics and beyond.

4. Experimental Section

Materials: Technical grade ODE (90%), DDT (99.9%), ODT (98%), OA (70%), antimony trichloride (SbCl$_3$, 99.999%), antimony triacetate Sb(AcO)$_3$ (99.99%), and antimony trifluoride SbF$_3$ (99.8%) were purchased from Sigma Aldrich. Chloroform was obtained from Alfa Aesar. HPLC grade chloroform was obtained from Scharlab. Isopropyl alcohol (IPA, 99.8%) was obtained from Panreac. DDT, ODE, and OA were dried with molecular sieves overnight, degassed at 110 °C under vacuum overnight (12 h) and store under argon before use. The dried and degassed solvents were used as feedstock for each injection.

Pre-Treatment of the SbCl$_3$: The synthesis of both the antimony precursor and the resulting antimonene was carried out following the methodology described by Peng et al.[16] For the SbCl$_3$-DDT precursor, SbCl$_3$ (0.912 g, 4 mmol), DDT (4 mL), and ODE (6 mL) were added into a 50 mL 3-neck flask, degassed under vacuum for 2 h at 110 °C, and purged with Ar. Afterward, the mixture was heated under Ar to 150 °C until all SbCl$_3$ reacted with DDT. The signal that the reaction had taken place was a color change from transparent to yellowish. Since SbCl$_3$-DDT precursor solution precipitated out of ODE at room temperature, it was preheated at 60 °C before its use.

Synthesis of Hexagonal Antimonene Nanosheets: In a typical synthesis, OA (0.5 mL), and ODE (4.0 mL) were added in a 50 mL three-necked flask. The reaction mixture was degassed under vacuum for 30 min at 110 °C and purged with argon. Next, the flask was heated up to 300 °C, and then 1 mL of SbCl$_3$-DDT precursor solution was injected swiftly into the reaction system. After 10 s, the reaction was stopped and cooled down by immersing the flask into a water bath, and the final FLA was obtained by centrifugation. In order to isolate the thickest nanosheets, the mixture was centrifuged twice at 13 400 rpm for 20 min and redispersed in CHCl$_3$.

Synthesis of Few Layer Antimonene Hexagons in Continuous Flow: The reaction medium, ODE and OA, were degassed under vacuum for 30 min at 110 °C. After that reaction medium and precursor, in a 5:1 ratio, were mixed under Ar in a flask. The tubular steel reactor used was 50 cm long, 6 mm internal diameter, and 8 mm external diameter and was heated up through Joule effect. The reactor was preheated at 250 °C, and then the mixture was pumped in the reactor by a peristaltic pump with an 11 mL min^{-1} flow. The product was cooled down at room temperature in the collector flask. FLA hexagons were centrifuged at 8000 rpm for 5 min. and washed with chloroform three times to remove the reaction solvents.

Supporting information provides a detailed description of the methods used in this work.

Supporting Information

Supporting Information is available from the Wiley Online Library or from the author.

Acknowledgements

Conflict of Interest

The authors declare no conflict of interest.

Data Availability Statement

Research data are not shared.

Keywords

[1] K. S. Novoselov, A. K. Geim, S. V. Morozov, D. Jiang, Y. Zhang, S. V. Dubonos, I. V. Grigorieva, A. A. Firsov, *Science* **2004**, *306*, 666.

[2] K. S. Novoselov, D. Jiang, F. Schedin, T. J. Booth, V. V. Khotkevich, S. V. Morozov, A. K. Geim, *Proc. Natl. Acad. Sci. U. S. A.* **2005**, *102*, 10451.

[3] Q. H. Wang, K. Kalantar-Zadeh, A. Kis, J. N. Coleman, M. S. Strano, *Nat. Nanotechnol.* **2012**, *7*, 699.

[4] B. Anasori, *Nat. Rev.* **2017**, *2*, 16098.

[5] L. Zhang, T. Gong, Z. Yu, H. Dai, Z. Yang, G. Chen, J. Li, R. Pan, H. Wang, Z. Guo, H. Zhang, X. Fu, *Adv. Funct. Mater.* **2021**, *31*, 2005471.

[6] a) S. Zhang, S. Guo, Z. Chen, Y. Wang, H. Gao, J. Gómez-Herrero, P. Ares, F. Zamora, Z. Zhu, H. Zeng, *Chem. Soc. Rev.* **2018**, *47*, 982; b) S. Guo, Y. Zhang, Y. Ge, S. Zhang, H. Zeng, H. Zhang, *Adv. Mater.* **2019**, *31*, 1902352.

[7] a) J. Pei, J. Yang, T. Yildirim, H. Zhang, Y. Lu, *Adv. Mater.* **2019**, *31*, 1706945; b) A. Castellanos-Gomez, L. Vicarelli, E. Prada, J. O. Island, K. L. Narasimha-Acharya, S. I. Blanter, D. J. Groenendijk, M. Buscema, G. A. Steele, J. V. Alvarez, H. W. Zandbergen, J. J. Palacios, H. S. J. van der Zant, *2D Mater.* **2014**, *1*, 025001; c) H. Liu, Y. Du, Y. Deng, P. D. Ye, *Chem. Soc. Rev.* **2015**, *44*, 2732.

[8] a) X. Wang, Y. Hu, J. Mo, J. Zhang, Z. Wang, W. Wei, H. Li, Y. Xu, J. Ma, J. Zhao, Z. Jin, Z. Guo, *Angew. Chem., Int. Ed.* **2020**, *59*, 5151; b) Y. Hu, Z.-H. Qi, J. Lu, R. Chen, M. Zou, T. Chen, W. Zhang, Y. Wang, X. Xue, J. Ma, Z. Jin, *Chem. Mater.* **2019**, *31*, 4524; c) Z.-H. Qi, Y. Hu, Z. Jin, J. Ma, *Phys. Chem. Chem. Phys.* **2019**, *21*, 12087; d) W. Zhang, Y. Hu, L. Ma, G. Zhu, P. Zhao, X. Xue, R. Chen, S. Yang, J. Ma, J. Liu, Z. Jin, *Nano Energy* **2018**, *53*, 808.

[9] a) E. Martínez-Periñán, M. P. Down, C. Gibaja, E. Lorenzo, F. Zamora, C. E. Banks, *Adv. Energy Mater.* **2018**, *8*, 1702606; b) V. Lloret, M. Á. Rivero-Crespo, J. A. Vidal-Moya, S. Wild, A. Doménech-Carbó, B. S. J. Heller, S. Shin, H.-P. Steinrück, F. Maier, F. Hauke, M. Varela, A. Hirsch, A. Leyva-Pérez, G. Abellán, *Nat. Commun.* **2019**, *10*, 509; c) X. Ren, Z. Li, H. Qiao, W. Liang, H. Liu, F. Zhang, X. Qi, Y. Liu, Z. Huang, D. Zhang, J. Li, J. Zhong, H. Zhang, *ACS Appl. Energy Mater.* **2019**, *2*, 4774; d) Y. Duo, Y. Huang, W. Liang, R. Yuan, Y. Li, T. Chen, H. Zhang, *Adv. Funct. Mater.* **2020**, *30*, 1906010; e) T. García-Mendiola, C. Gutiérrez-Sánchez, C. Gibaja, I. Torres, C. Busó-Rogero, F. Pariente, J. Solera, Z. Razavifar, J. J. Palacios, F. Zamora, E. Lorenzo, *ACS Appl. Nano Mater.* **2020**, *3*, 3625.

[10] a) Y. Wang, W. Huang, C. Wang, J. Guo, F. Zhang, Y. Song, Y. Ge, L. Wu, J. Liu, J. Li, H. Zhang, *Laser Photonics Rev.* **2019**, *13*, 1800313; b) J. He, L. Tao, H. Zhang, B. Zhou, J. Li, *Nanoscale* **2019**, *11*, 2577.

[11] N. Antonatos, H. Ghodrati, Z. Sofer, *Appl. Mater. Today* **2020**, *18*, 100502.

[12] P. Ares, F. Aguilar-Galindo, D. Rodríguez-San-Miguel, D. A. Aldave, S. Díaz-Tendero, M. Alcamí, F. Martín, J. Gómez-Herrero, F. Zamora, *Adv. Mater.* **2016**, *28*, 6332.

[13] a) J. Ji, X. Song, J. Liu, Z. Yan, C. Huo, S. Zhang, M. Su, L. Liao, W. Wang, Z. Ni, Y. Hao, H. Zeng, *Nat. Commun.* **2016**, *7*, 13352;

b) X. Wu, Y. Shao, H. Liu, Z. Feng, Y.-L. Wang, J.-T. Sun, C. Liu, J.-O. Wang, Z.-L. Liu, S.-Y. Zhu, Y.-Q. Wang, S.-X. Du, Y.-G. Shi, K. Ibrahim, H.-J. Gao, *Adv. Mater.* **2017**, *29*, 1605407.

[14] a) C. Gibaja, D. Rodriguez-San-Miguel, P. Ares, J. Gómez-Herrero, M. Varela, R. Gillen, J. Maultzsch, F. Hauke, A. Hirsch, G. Abellán, F. Zamora, *Angew. Chem., Int. Ed.* **2016**, *55*, 14345; b) C. Gibaja, M. Assebban, I. Torres, M. Fickert, R. Sanchis-Gual, I. Brotons, W. S. Paz, J. J. Palacios, E. G. Michel, G. Abellán, F. Zamora, *J. Mater. Chem. A* **2019**, *7*, 22475.

[15] M. Assebban, C. Gibaja, M. Fickert, I. Torres, E. Weinreich, S. Wolff, R. Gillen, J. Maultzsch, M. Varela, S. Tan Jun Rong, K. P. Loh, E. G. Michel, F. Zamora, G. Abellán, *2D Mater.* **2020**, *7*, 025039.

[16] L. Peng, S. Ye, J. Song, J. Qu, *Angew. Chem., Int. Ed.* **2019**, *58*, 9891.

[17] a) A. Biswas, I. S. Bayer, A. S. Biris, T. Wang, E. Dervishi, F. Faupel, *Adv. Colloid Interface Sci.* **2012**, *170*, 2. b) R. G. Hobbs, N. Petkov, J. D. Holmes, *Chem. Mater.* **2012**, *24*, 1975.

[18] L. Lu, X. Tang, R. Cao, L. Wu, Z. Li, G. Jing, B. Dong, S. Lu, Y. Li, Y. Xiang, J. Li, D. Fan, H. Zhang, *Adv. Opt. Mater.* **2017**, *5*, 1700301.

[19] a) M. A. Uddin, J. K. Mobley, A. A. Masud, T. Liu, R. L. Calabro, D.-Y. Kim, C. I. Richards, K. R. Graham, *J. Phys. Chem. C* **2019**, *123*, 18103; b) J. Huang, Y.-H. Wu, Z.-G. Zhu, W. Y. Shih, W.-H. Shih, *Chem. Phys. Lett.* **2018**, *702*, 21.

[20] a) S. Ithurria, G. Bousquet, B. Dubertret, *J. Am. Chem. Soc.* **2011**, *133*, 3070; b) K. P. Rice, A. E. Saunders, M. P. Stoykovich, *J. Am. Chem. Soc.* **2013**, *135*, 6669.

[21] J. Zhang, S. Ye, Y. Sun, F. Zhou, J. Song, J. Qu, *Nanoscale* **2020**, *12*, 20945.

[22] a) S. Mourdikoudis, L. M. Liz-Marzán, *Chem. Mater.* **2013**, *25*, 1465; b) J. De Roo, M. Ibáñez, P. Geiregat, G. Nedelcu, W. Walravens, J. Maes, J. C. Martins, I. Van Driessche, M. V. Kovalenko, Z. Hens, *ACS Nano* **2016**, *10*, 2071.

[23] S. E. Lohse, N. D. Burrows, L. Scarabelli, L. M. Liz-Marzán, C. J. Murphy, *Chem. Mater.* **2014**, *26*, 34.

[24] H. Lim, C. Carraro, R. Maboudian, M. W. Pruessner, R. Ghodssi, *Langmuir* **2004**, *20*, 743.

[25] Q. Wang, X. Yang, J. Hou, M. Huang, Y. Zhao, *Appl. Surf. Sci.* **2011**, *257*, 5857.

[26] a) S. D. Perrault, W. C. W. Chan, *J. Am. Chem. Soc.* **2009**, *131*, 17042; b) N. G. Bastús, J. Comenge, V. Puntes, *Langmuir* **2011**, *27*, 11098.

[27] M. Fickert, M. Assebban, J. Canet-Ferrer, G. Abellán, *2D Mater.* **2020**, *8*, 015018.

[28] S. Wolff, R. Gillen, M. Assebban, G. Abellán, J. Maultzsch, *Phys. Rev. Lett.* **2020**, *124*, 126101.

[29] P. Schweizer, C. Dolle, D. Dasler, G. Abellán, F. Hauke, A. Hirsch, E. Spiecker, *Nat. Commun.* **2020**, *11*, 1743.

[30] a) P. Ares, J. J. Palacios, G. Abellán, J. Gómez-Herrero, F. Zamora, *Adv. Mater.* **2018**, *30*, 1703771; b) M. Fortin-Deschênes, O. Waller, T. O. Menteş, A. Locatelli, S. Mukherjee, F. Genuzio, P. L. Levesque, A. Hébert, R. Martel, O. Moutanabbir, *Nano Lett.* **2017**, *17*, 4970.

[31] R. Kappera, D. Voiry, S. E. Yalcin, B. Branch, G. Gupta, A. D. Mohite, M. Chhowalla, *Nat. Mater.* **2014**, *13*, 1128.